JOURNAL OF SPACECRAFT AND ROCKETS
Vol. 46, No. 4, July–August 2009

Virtual Air Data System Architecture for Space Reentry Applications

Francesco Nebula,* Roberto Palumbo,† Gianfranco Morani,‡ and Federico Corraro§
Italian Aerospace Research Center, 81043 Capua, Italy

DOI: 10.2514/1.42485

In this paper, an advanced air data system architecture based on the concept of virtual air data is proposed. Virtual air data are virtual measurements based on the combination of inertial measurements with weather forecast data coming from a meteorological model. This model can be considered as a virtual sensor that provides information on wind velocities, air temperature, and air pressure. The combination of inertial measurements with weather forecast data has been carried out using a sensor fusion algorithm (specifically, an extended Kalman filter) allowing the estimation of the true-air-speed components. This kind of air data system architecture allows most of the typical limitations of conventional air data probes to be overcome and does not require any specific experimental or computational fluid dynamics calibration campaign or any thermal protection system when dealing with reentry applications. Its effectiveness has been demonstrated with two practical applications, the first based on the postflight analysis of the first Dropped Transonic Flight Test mission (carried out by the Italian Aerospace Research Center) and the second based on a simulated case of the second Dropped Transonic Flight Test planned for the next years.

Nomenclature

$\underline{C}_{F_a}^{\mathrm{ADB}}$	=	aerodynamic force coefficients in stability axes
$\underline{F}_a$	=	aerodynamic force acting on the vehicle, N
f	=	system transition function
g^{WGS84}	=	acceleration of gravity according to the WGS84 model, m/s^2
H	=	measured altitude, m
H_{δ_e}, H_{δ_n}	=	autocorrelation lengths of low-frequency wind prediction error, m
h	=	system output function
$L_{\Delta u}$, $L_{\Delta v}$, $L_{\Delta w}$	=	turbulence scale lengths, ft
M	=	Mach number
$\underline{M}_{b2n}$	=	measured body to north–east–down rotation matrix
$\underline{M}_{s2b}$	=	stability to body rotation matrix
m	=	vehicle mass, kg
$\underline{ng}_{\mathrm{body}}$	=	measured body accelerations, m/s^2
p_s	=	static pressure, Pa
$\underline{Q}_k$, $\underline{Q}'$	=	process noise covariance matrices
R	=	specific gas constant of air (287.05 J/kg/K)
Re	=	Reynolds number
$\underline{R}_k$, $\underline{R}'$	=	measurement noise covariance matrices
R_{δ_e}, R_{δ_n}	=	autocorrelations of low-frequency wind prediction error
S_{ref}	=	reference surface, m^2
TAS	=	true air speed, m/s
T_s	=	static temperature, K
u, v, w	=	body true-air-speed components, m/s
V_{NED}	=	inertial velocity vector, m/s
$\underline{v}$, $\underline{w}$	=	white Gaussian noise vectors
W_{NE}	=	horizontal wind velocity vector, m/s
$\underline{x}$	=	state vector, output vector
$\underline{z}$	=	measurement vector
α	=	angle of attack, deg
β	=	sideslip angle, deg
γ	=	specific heats ratio of air, 1.4
$\underline{\Delta}$	=	turbulence velocity vector, m/s
$\underline{\delta}$	=	European Centre for Medium Range Weather Forecast wind prediction error, m/s
δ_{elev}	=	measured elevon deflections, deg
δ_{rud}	=	measured rudder deflections, deg
σ_{δ_e}, σ_{δ_n}	=	rms intensities of the low-frequency wind prediction error, m/s
$\sigma_{\Delta u}$, $\sigma_{\Delta v}$, $\sigma_{\Delta w}$	=	turbulence rms intensities, m/s
τ_{δ_e}, τ_{δ_n}	=	autocorrelation time constants of the low-frequency wind prediction error, s
$\Phi_{\Delta u}$, $\Phi_{\Delta v}$, $\Phi_{\Delta w}$	=	turbulence power density spectra (function of the temporal frequency), m^2/s
$\phi_{\Delta u}$, $\phi_{\Delta v}$, $\phi_{\Delta w}$	=	power density spectra of the turbulence model (function of the spatial frequency), m^3/s^2
ϕ_{δ_e}, ϕ_{δ_n}	=	power density spectra of the low-frequency wind prediction error, m^2/s
φ, ϑ, ψ	=	Euler angles, rad
Ω	=	spatial frequency, m^{-1}
ω	=	temporal frequency, s^{-1}
$\underline{\omega}_{\mathrm{body}}$	=	measured body angular rates, deg /s

Subscripts

b	=	body frame
n	=	north–east–down frame
stab	=	stability frame

Superscripts

l	=	left
meas	=	measured
r	=	right

Presented as Paper 6995 at the AIAA Guidance, Navigation, and Control Conference and Exhibit, Honolulu HI, 18–21 August 2008; received 1 December 2008; revision received 19 March 2009; accepted for publication 19 March 2009.

*Researcher, Flight System Department; f.nebula@cira.it.
†Researcher, Flight System Department; r.palumbo@cira.it. Member AIAA.
‡Researcher, Flight System Department; g.morani@cira.it.
§Senior Researcher, Flight System Department; f.corraro@cira.it.

I. Introduction

AIR data systems (ADS) consist of a set of aerodynamic and thermodynamic sensors and associated electronics that are used to obtain measurements of the asymptotic airflow and to determine flight parameters often required for guidance, navigation, and control

(GN&C) purposes [1]. All of the air data parameters that are relevant to flight performance are derived by sensing static and total pressures, total temperature, and aerodynamic flow angles (angle of attack and sideslip angle). These measurements are then processed to obtain some other useful air data (true air speed, Mach number, barometric altitude, etc.) using mathematical relationships of the gas dynamics (usually the laws of the isentropic flow) and using a prefixed atmospheric model (US62, for example). These formulas are implemented in a dedicated computation unit named the air data computer (ADC). In a reentry mission, these data become particularly important, especially in the last phases of flight [terminal area energy management (TAEM) and approach and landing] when the Mach number becomes relatively low. In fact, in this regime, the inertial velocity is comparable with the wind velocity, and the exclusive use of inertial platform measurements may lead to excessive approximations when determining air data quantities.

Conventional ADS are based on raw measurements of static and total pressures and of local flow angles using, respectively, static ports, pitot tubes, and angle-of-attack and sideslip vanes. These kinds of probes (except for the static pressure port) are said to be *intrusive,* because they disturb the local airflow. These disturbances, together with the disturbances introduced by the vehicle, generate measurement errors that can be compensated only through an extensive calibration campaign via computational fluid dynamics (CFD) calculations, wind-tunnel tests, and flight experimentation. Moreover, traditional air data booms are sensitive to vibrations and alignment errors and are easily damaged in flight or on the ground.

When performing space reentry missions or, more generally, hypersonic flights, conventional ADS probes are inadequate, primarily because of the high temperatures that the vehicle experiences. Indeed, sharp edges and small radii of curvature of pitot tubes and wind vanes make these sensors inherently unsuitable for the harsh thermal environment of a reentry flight [2]. In addition, shock wave formation significantly changes the pressure and the velocity of the flow encountered by the probes, thus altering the measurements. These phenomena are amplified when the probes are too intrusive. Furthermore, even at low Mach numbers, particular vehicle attitudes (large angles of attack or sideslip) or dynamic maneuvers may degrade the performance of traditional air data probes, thus requiring a different approach to air data sensing.

Over the years, several efforts have been made to design *nonintrusive* probes suitable for hypersonic flights and reentry vehicles. The first major attempt to collect air data on a hypersonic vehicle was the ball-nose flow-direction sensor on the X-15 research vehicles (further details can be found in [3,4]). The ball-nose sensor consisted of a sphere partly housed in a truncated cone nose. A hydraulic servomechanism rotated the sphere to maintain pressure differentials between symmetric (vertical and lateral) flush orifice pairs at null values. Thus, the sphere was positioned in flight such that the center orifice sensed total pressure and the rotation angles of the ball nose corresponded approximately to flow angles. Static pressure was sensed from two fuselage static orifices used in conjunction with the ball nose [2]. High-stagnation-temperature protection was provided through the use of a cooling system. Although this kind of sensor was subject to frequent (hydraulic) failures [4,5], its performance appeared to be adequate to monitor hypersonic and supersonic flight parameters.

The ball-nose system was abandoned when the X-15 project was concluded. In the 1980s, the Shuttle Entry Air Data System (SEADS) program was proposed. Its main objective was to design an ADS based on the use of flush-mounted orifices, but unlike the ball nose, without any mechanical device, and able to determine flight parameters in a broader range of hypersonic and supersonic conditions than those for the shuttle's deployable hemispherical probes [2]. The SEADS was flight-tested as an experiment on Space Shuttle *Columbia* and employed an array of 14 flush-mounted pressure transducers on the nose cap and 6 static pressure ports on the aft of the nose cap [1,2,5]. Pressure measurements were then related to the air data quantities through a mathematical model of the pressure distribution on the orbiter forebody. Actually, the SEADS was never used to provide flight parameters to the shuttle: pressure data were stored and were analyzed during postflight. In fact, up to this date, the Space Shuttle Orbiter still relies exclusively on air data provided by two conventional fuselage-mounted differential pressure probes that are deployed at Mach 3.5 [2]. For higher Mach numbers, air data parameters are estimated from the inertially derived navigation state (which implicitly and inaccurately assumes zero winds). Both air data systems described previously verified the feasibility of the flush air data sensing (FADS) system but did not demonstrate real-time operation of its estimation algorithms. Real-time applications were developed successively, within the framework of the High-Alpha Research Vehicle program [6] and within the framework of the X-33, X-38, and X-43 hypersonic research vehicles [7–9].

Recent studies demonstrate that, at least in a simulated environment, blending FADS data with inertial measurements allows achieving clean and unbiased air data measurements over the entire reentry flight envelope [5]. Other types of nonintrusive probes include the optical air data systems (OADS). Basically, these kinds of sensors transmit laser light pulses into the atmosphere and receive light that is reflected, or backscattered, from aerosols toward the aircraft. Measurement of the Doppler shift and of other characteristics of the backscattered signal allows the determination of the true air speed, air temperature, and air density [1,10]. OADS and the more recent molecular optical air data systems have shown promising and accurate results in different flight conditions from high-angle-of-attack maneuvers to hover flights [11].

In any case, current nonintrusive ADS, despite overcoming most of the limitations of the traditional ADS, still require calibration campaigns and thermal protection for hypersonic flights. Moreover, sensing devices may introduce a number of technological issues in terms of installation on the vehicle, reliability, or even safety when dealing with laser measurement systems (eye and skin hazards) [11].

In this paper, starting from the limitations and problems of the conventional ADS and taking advantage of our flight experience acquired during the Dropped Transonic Flight Test 1 (DTFT1) [12], an alternative architecture for an advanced nonintrusive ADS is proposed. This novel approach is based on a sensor fusion between inertial measurements and atmospheric data coming from a weather forecast model that acts essentially as a *virtual* sensor. This architecture, conceptually a virtual air data (VAD) system, being based on the use of nonphysical air data sensors, is inherently free from issues that might arise when using either conventional or nonintrusive ADS, especially during reentry missions. In fact, it has the advantage of neither requiring any calibration campaign nor any thermal protection of the sensing devices.

The work developed in this paper, although preliminary, aims at assessing the feasibility of this architecture to provide air data with the required accuracy for guidance, navigation, and control purposes. Originally, this new ADS approach was conceived with the intention of overcoming the measurement errors experienced during the DTFT1 mission due to the use of conventional air data sensors (initial large oscillations of the wind vanes, delayed pressure signals with irregular behavior in the transonic regime with negative effects on the Mach measurement, and freezing of the total temperature probe).

The DTFT1 test flight is the first of three planned atmospheric flights within the framework of the research program named Unmanned Space Vehicles (USV) carried out by the Italian Aerospace Research Center (CIRA) [12]. The main focus of the USV program is primarily related to aerodynamic and aerostructural behavior and to advanced GN&C systems for transonic, supersonic, and sustained hypersonic flights. The USV program is divided into two parts, the first of which deals with flight and operation issues related to typical flight regimes of the TAEM phase of a reentry pattern, and the second of which is concerned with sustained hypersonic flights. In particular, the DTFT1 mission profile is based on a drop of an experimental, unpowered, and autonomous vehicle, the FTB1, from a stratospheric balloon at an altitude of about 20 km. The FTB1 vehicle has a winged slender configuration, with two kinds of aerodynamic effectors: the elevons that provide both pitch control when deflected symmetrically and roll control when deflected asymmetrically and the rudders, which can be deflected only symmetrically to allow yaw control. Lateral-directional stability

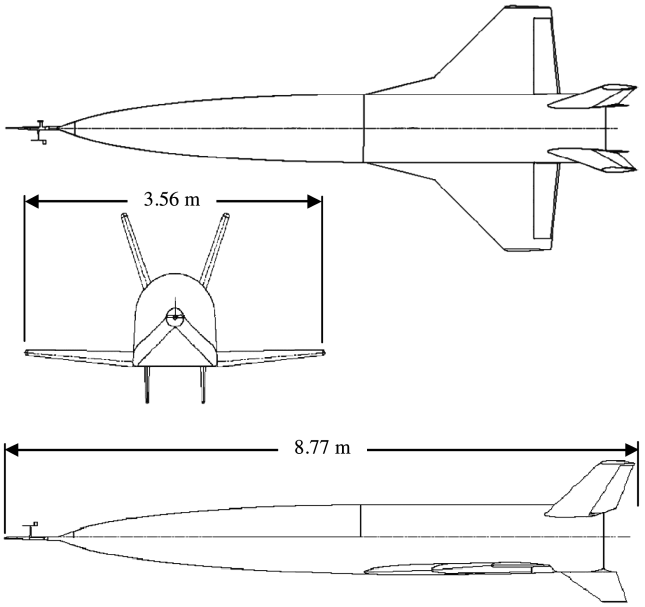

Fig. 1 FTB1 vehicle.

is also enhanced by means of two fixed ventral fins (see Fig. 1). The DTFT1 mission was executed on 24 February 2007 and further details may be found in [12–14].

The present work demonstrates the capability of the VAD architecture only within the flight envelope of the DTFT1 mission and within the simulated flight envelope of the upcoming DTFT2 mission. Nevertheless, the authors believe that future USV missions will demonstrate the capability of the VAD to work in a broader flight envelope. In addition, current work is focusing on the implementation of the VAD for in-flight use as the main air data sensor system for GN&C purposes during the DTFT2 mission.

This paper is organized as follows. The general concept of virtual air data is introduced in Sec. II. The characterizations of the wind forecast error and of wind turbulence are reported in Sec. III. The sensor fusion algorithm is described in Sec. IV, and the results of this work are discussed in Sec. V. Section VI contains some comments on applications and future enhancements, and Sec. VII contains some brief concluding remarks.

II. Virtual Air Data

The VAD concept is based essentially on the combination of inertial measurements with meteorological forecast data via a sensor fusion algorithm, with the purpose of obtaining an estimation (virtual measurement) of the air data quantities.

The inertial measurements necessary for the determination of the virtual measurements are position and velocity, which can be computed using accelerometers, and Euler angles, which can be determined using rate gyros and magnetometers or can be directly provided by an attitude and heading reference system (AHRS).

The weather forecast data consist of wind velocity components in the local horizontal plane, the atmospheric temperature, and the atmospheric pressure, all expressed as a function of the inertial position of the vehicle. These quantities can be provided by any meteorological model. In particular, in the development of this work, the forecast data of the Integrated Forecast System (IFS) numerical model by the European Centre for Medium Range Weather Forecast (ECMWF) have been used.

Figure 2 shows the functional architecture of the virtual air data concept. The meteorological (forecast) model can be seen as a virtual sensor that supplies atmospheric data with a known accuracy. These data have the advantage that can be easily uploaded before the mission starts or, for space reentry missions, before deorbiting operations.

A. Basic Virtual Air Data

As stated in the Introduction, the plain estimation of the air data quantities using only inertial measurements (zero-wind estimation) can be extremely inaccurate when inertial velocity and wind velocity are comparable. The easiest possible approach to virtual air data estimation is the simple algebraic combination of wind forecast data and inertial measurements; that is, the inertial velocity is algebraically summed to the wind forecast to obtain an estimate of the wind-relative velocity. This basic sensor fusion (basic VAD) yields virtual air data measurements that are certainly more reliable and accurate than the plain zero-wind estimation. Of course, this basic estimation is affected by errors on the weather forecast model and on the inertial measurements. These errors are not taken into account in this simple sensor fusion algorithm. However, the basic virtual air data measurements give a good and straightforward indication of the validity of the virtual sensor approach (some results are reported in Sec. V). Therefore, the estimation method has been improved through the implementation of a more advanced sensor fusion algorithm, which will be the main subject of this paper.

B. Advanced Virtual Air Data

The advanced VAD system architecture consists of a sensor fusion algorithm that blends, via a Kalman filter (KF), the inertial measurements with weather forecast data while taking into account measurement errors, modeling errors, and the uncertainties on the ECMWF predictions. Indeed, the errors on the IFS weather forecast model have been statistically characterized through an extensive analysis of historical meteorological data (see [15]). This characterization, however, does not account for errors due to local and unsteady wind phenomena (turbulence and gusts) existing in the true wind because of the large spatial sampling of these data. Therefore, an appropriate dynamic wind error model should be introduced to improve the results. In particular, the high-frequency component of the true-air-speed error can be characterized using a well-known turbulence dynamic model such as the Dryden spectral representation.

III. Characterization of the Wind Prediction Error

In this section, the characterization of the wind velocity prediction error will be carried out. As previously described, the wind velocity provided by the IFS weather forecast data is obviously affected by an

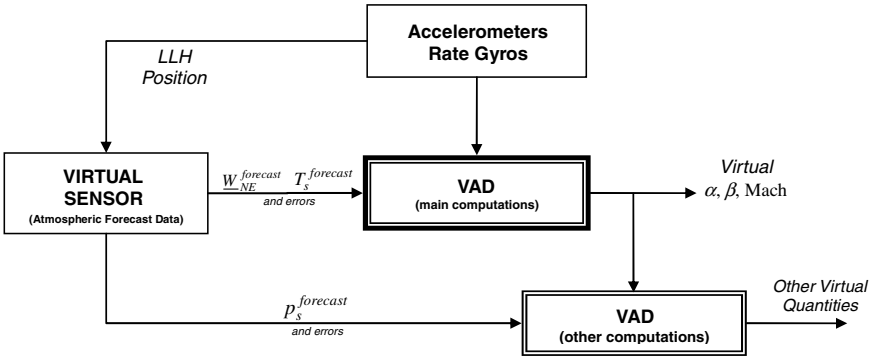

Fig. 2 Virtual air data functional architecture.

estimation error, which is the difference between the true and the estimated wind. This error, hereafter called the low-frequency prediction error, has been statistically characterized through an analysis of historical meteorological data: that is, comparing the ECMWF forecast data with historical analysis data [15]. This characterization provides a wind-prediction-error model that can be used by the sensor fusion algorithm described in the following section. However, as previously remarked, the preceding characterization is not capable of accounting for unsteady phenomena, because of the nature of the available meteorological data. Therefore, to achieve a complete characterization of the wind prediction error, a turbulence dynamic model is also needed.

A. Low-Frequency Wind Prediction Error

The error due to the ECMWF forecast uncertainty (low-frequency error) $\underline{\delta} = (\,\delta_e \quad \delta_n\,)^T$ depends on the inertial position of the vehicle. Nevertheless, its characterization has been carried out considering the error to be independent of latitude and longitude. This assumption can be justified considering that above a certain altitude, the wind prediction error is mainly due to the wind model inaccuracy and not to the specific geography of the site [15]. Furthermore, a first-order Gauss–Markov stochastic model [16,17] has been used with the following altitude autocorrelation function:

$$R_{\delta_e}(\xi) = \sigma_{\delta_e}^2 e^{-\frac{|\xi|}{H_{\delta_e}}} \qquad R_{\delta_n}(\xi) = \sigma_{\delta_n}^2 e^{-\frac{|\xi|}{H_{\delta_n}}} \tag{1}$$

where H_{δ_e} and H_{δ_n} are the autocorrelation scale lengths, and σ_{δ_e} and σ_{δ_n} are the error rms intensities. Now considering an aircraft flying with a vertical velocity V_z, these models can be easily transformed into standard stochastic processes with autocorrelation time constants $\tau_{\delta_e} = H_{\delta_e}/V_z$ and $\tau_{\delta_n} = H_{\delta_n}/V_z$,

$$R_{\delta_e}(\tau) = \sigma_{\delta_e}^2 e^{-\frac{|\tau|}{\tau_{\delta_e}}} \qquad R_{\delta_n}(\tau) = \sigma_{\delta_n}^2 e^{-\frac{|\tau|}{\tau_{\delta_n}}} \tag{2}$$

and power density spectra

$$\begin{aligned}\phi_{\delta_e}(j\omega) &= \sigma_{\delta_e}^2 \frac{2/\tau_{\delta_e}}{(1/\tau_{\delta_e}^2) + \omega^2} = \sigma_{\delta_e}^2 \frac{2}{\tau_{\delta_e}} |H_{\delta_e}(j\omega)|^2 \\ \phi_{\delta_n}(j\omega) &= \sigma_{\delta_n}^2 \frac{2/\tau_{\delta_n}}{(1/\tau_{\delta_n}^2) + \omega^2} = \sigma_{\delta_n}^2 \frac{2}{\tau_{\delta_n}} |H_{\delta_n}(j\omega)|^2\end{aligned} \tag{3}$$

where

$$H_{\delta_e}(j\omega) = \frac{1}{(1/\tau_{\delta_e}) + j\omega}$$

$$H_{\delta_n}(j\omega) = \frac{1}{(1/\tau_{\delta_n}) + j\omega}$$

The parameters τ_{δ_e}, τ_{δ_n}, $\sigma_{\delta_e}^2$, and $\sigma_{\delta_n}^2$ in Eq. (2) have been determined by fitting the experimental autocorrelation functions (computed through a statistical analysis of historical data) with the models of Eqs. (1).

B. Turbulence Model

To characterize the turbulence components to be added to the TAS body vector, a turbulence dynamic model has been introduced. The most widely used turbulence models are Dryden and von Kármán models, which define three power density spectra for the body axes' turbulence velocities $\underline{\Delta} = (\,\Delta u \quad \Delta v \quad \Delta w\,)^T$.

In this paper, the Dryden model will be used; in fact, even if the von Kármán model is more reliable [18], the Dryden model has the great advantage of being simpler and hence more suitable to achieve an analytical form necessary for the linearization process required by the methodology herein presented (see Sec. IV). The power density spectra of the Dryden turbulence model are then given in Eq. (4):

$$\begin{aligned}\phi_{\Delta u}(\Omega) &= \sigma_{\Delta u}^2 \frac{2L_{\Delta u}}{\pi} \frac{1}{1 + (L_{\Delta u}\Omega)^2} \\ \phi_{\Delta v}(\Omega) &= \sigma_{\Delta v}^2 \frac{L_{\Delta v}}{\pi} \frac{1 + 3(L_{\Delta v}\Omega)^2}{[1 + (L_{\Delta v}\Omega)^2]^2} \\ \phi_{\Delta w}(\Omega) &= \sigma_{\Delta w}^2 \frac{L_{\Delta w}}{\pi} \frac{1 + 3(L_{\Delta w}\Omega)^2}{[1 + (L_{\Delta w}\Omega)^2]^2}\end{aligned} \tag{4}$$

where Ω is the spatial frequency; $L_{\Delta u}$, $L_{\Delta v}$, and $L_{\Delta w}$ are the turbulence scale lengths; and $\sigma_{\Delta u}$, $\sigma_{\Delta v}$, and $\sigma_{\Delta w}$ are the turbulence rms intensities. The spectrum parameters $L_{\Delta u}$, $L_{\Delta v}$, and $L_{\Delta w}$ and $\sigma_{\Delta u}$, $\sigma_{\Delta v}$, and $\sigma_{\Delta w}$ are altitude-dependent, but above 2000 ft, the following assumption can be made [18]:

$$L_{\Delta u} = L_{\Delta v} = L_{\Delta w} = \bar{L} \qquad \sigma_{\Delta u} = \sigma_{\Delta v} = \sigma_{\Delta w} = \bar{\sigma}(H^{\text{meas}}) \tag{5}$$

where $\bar{L} = 1750$ ft and $\bar{\sigma}(H^{\text{meas}})$ is a known function of the altitude and of the turbulence level (severe, moderate, light, etc.) identified with an exceedance probability.

The preceding described power turbulence model should be converted into a stochastic process, as done for the ECMWF forecast error. Hence, starting from the preceding defined power spectra and considering an aircraft flying with a true air speed V, it is possible to obtain the following spectral density as a function of the temporal frequency $\omega = \Omega V$ by exploiting the following equality,

$$\begin{aligned}\int_{-\infty}^{+\infty} \phi_x(\Omega)\mathrm{d}\Omega = \int_{-\infty}^{+\infty} \Phi_x(\omega)\mathrm{d}\omega = \sigma_x^2 \Rightarrow \Phi_x(\omega) \\ = \frac{\phi_x(\Omega)|_{\Omega=\frac{\omega}{V}}}{V} \qquad x = \Delta u, \Delta v, \Delta w\end{aligned} \tag{6}$$

thus obtaining the following Dryden power spectral densities:

$$\begin{aligned}\Phi_{\Delta u}(\omega) &= \bar{\sigma}^2 \frac{2}{\pi} \tau_\Delta \frac{1}{1 + (\omega\tau_\Delta)^2} = \bar{\sigma}^2 \frac{2}{\pi} \tau_\Delta |H_{\Delta u}(\omega)|^2 \\ \Phi_{\Delta v}(\omega) &= \bar{\sigma}^2 \frac{\tau_\Delta}{\pi} \frac{1 + 3(\omega\tau_\Delta)^2}{[1 + (\omega\tau_\Delta)^2]^2} = \bar{\sigma}^2 \frac{\tau_\Delta}{\pi} |H_{\Delta v}(\omega)|^2 \\ \Phi_{\Delta w}(\omega) &= \bar{\sigma}^2 \frac{\tau_\Delta}{\pi} \frac{1 + 3(\omega\tau_\Delta)^2}{[1 + (\omega\tau_\Delta)^2]^2} = \bar{\sigma}^2 \frac{\tau_\Delta}{\pi} |H_{\Delta w}(\omega)|^2\end{aligned} \tag{7}$$

where

$$H_{\Delta u}(\omega) = \frac{1}{1 + j\omega\tau_\Delta}$$

$$H_{\Delta v}(\omega) = \frac{1 + \sqrt{3}\tau_\Delta j\omega}{(1 + j\omega\tau_\Delta)^2}$$

$$H_{\Delta w}(\omega) = \frac{1 + \sqrt{3}\tau_\Delta j\omega}{(1 + j\omega\tau_\Delta)^2}$$

and $\tau_\Delta = \frac{\bar{L}}{V}$.

IV. Kalman Filter

Using the translational dynamics of the rigid body together with the forecast wind error model and the turbulence model described in Sec. III, it is possible to obtain a state-space model that can predict, stochastically, the time evolution of the inertial velocity $\underline{V}_{\text{NED}}$, the low-frequency prediction error $\underline{\delta} = (\,\delta_e \quad \delta_n\,)^T$, and the turbulence body components $\underline{\Delta} = (\,\Delta u \quad \Delta v \quad \Delta w\,)^T$. Note that the wind velocity plays a crucial role (see Fig. 3) because it affects not only the aerodynamic forces and the dynamic pressure (through TAS and Mach), but also directly affects the TAS itself (and therefore the flow angles and the Mach number). Therefore, it is clear that the wind must be properly identified both in its low-frequency and in its turbulence content to provide a TAS that is as close to reality as it can get.

Traditionally, air data systems provide a direct measurement of the TAS vector. In a VAD system instead, TAS is computed using the

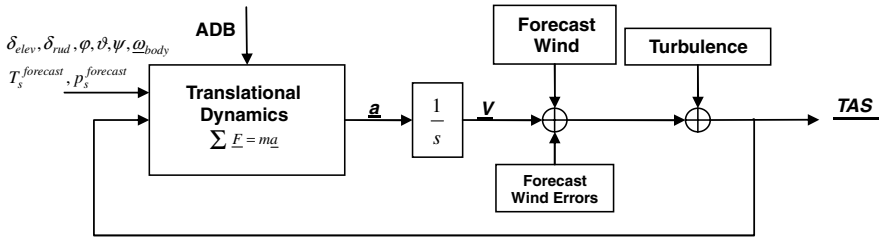

Fig. 3 Virtual air data main computation flow.

$$\underline{M}_{b2n}^{\text{meas}} = (\underline{M}_{n2b}^{\text{meas}})^T = \begin{pmatrix} \cos\vartheta\cos\psi & -\sin\psi\cos\varphi + \cos\psi\sin\vartheta\sin\varphi & \sin\psi\sin\varphi + \cos\psi\sin\vartheta\cos\varphi \\ \sin\psi\cos\vartheta & \cos\psi\cos\varphi + \sin\psi\sin\vartheta\sin\varphi & -\cos\psi\sin\varphi + \sin\psi\sin\vartheta\cos\varphi \\ -\sin\vartheta & \cos\vartheta\sin\varphi & \cos\vartheta\cos\varphi \end{pmatrix} \tag{10}$$

forecast wind corrected for prediction errors, the turbulence components, and the inertial velocity components, which are obtained through the integration of the translational dynamics equations. This integration, however, requires the knowledge of the aerodynamic database (ADB) necessary to compute the aerodynamic forces. Such an ADB is provided by means of a mathematical model with a given accuracy that can be improved using some inertial measurements to perform corrections. The degree of such correction is usually related to the level of confidence that one gives to both the measurements and the mathematical model itself. A methodology that is based on this principle is the well-known KF approach [19,20]. It is capable of providing the optimal state estimation of an uncertain dynamic model in the presence of measurements affected by errors.

The reference systems are as follows:

1) The north–east–down (NED)-oriented frame is the local horizontal reference system.

2) The body frame is centered in the center of gravity of the vehicle, with the x axis lying along the longitudinal axis (forward-oriented), the z axis in the symmetry plane (down-oriented), and the y axis consequently oriented to the right wing.

3) The stability frame is obtained by rotating the body frame about the y axis of the angle of attack.

The continuous nonlinear state-space model used for the KF formulation is introduced:

$$\frac{d\underline{x}}{dt} = \frac{d}{dt}\begin{pmatrix} \underline{V}_{\text{NED}} \\ \delta_e \\ \delta_n \\ \Delta u \\ \Delta v \\ \Delta w \\ \Delta v_1 \\ \Delta w_1 \end{pmatrix} = \underline{f}(\underline{x}, \underline{u}, t) + \underline{w}(t)$$

$$= \begin{pmatrix} \underline{F}_{a_{\text{NED}}}/m + (0 \quad 0 \quad g^{\text{WGS84}})^T \\ -\delta_e/\tau_{\delta_e} \\ -\delta_n/\tau_{\delta_n} \\ -\Delta u/\tau_\Delta \\ -\frac{\Delta v}{\tau_\Delta} + (\frac{1-\sqrt{3}}{\tau_\Delta})\Delta v_1 \\ -\frac{\Delta w}{\tau_\Delta} + (\frac{1-\sqrt{3}}{\tau_\Delta})\Delta w_1 \\ -\Delta v_1/\tau_\Delta \\ -\Delta w_1/\tau_\Delta \end{pmatrix} + \underline{w}(t) \tag{8}$$

$$\underline{z}(t) = \underline{g}(\underline{x}, \underline{u}, t) + \underline{v}(t) \tag{9}$$

where:

$$\underline{M}_{s2b} = \begin{pmatrix} \cos\alpha & 0 & -\sin\alpha \\ 0 & 1 & 0 \\ \sin\alpha & 0 & \cos\alpha \end{pmatrix} \tag{11}$$

$$\underline{F}_{a_{\text{NED}}} = \underline{M}_{b2n}^{\text{meas}}(\underline{M}_{s2b}\underline{F}_{a_{\text{stab}}}) \tag{12}$$

$$\underline{F}_{a_{\text{stab}}} = \underline{C}_{F_a}^{\text{ADB}}\left(\frac{\gamma}{2}p_s^{\text{forecast}}M^2\right)S_{\text{ref}} \tag{13}$$

$$\underline{C}_{F_a}^{\text{ADB}} = \underline{C}_{F_a}^{\text{ADB}}(\alpha, \beta, M, Re, \delta_{\text{elev}}^r, \delta_{\text{elev}}^l, \delta_{\text{rud}}, \underline{\omega}_{\text{body}}^{\text{meas}}) \tag{14}$$

$$\underline{\text{TAS}}_{\text{NED}}^{\text{no turb}} = \underline{V}_{\text{NED}} - (\underline{W}_{\text{NE}}^{\text{forecast}} + \underline{\delta}) \tag{15}$$

$$\underline{\text{TAS}}_{\text{body}} = (\,u \quad v \quad w\,)^T = \underline{M}_{n2b}^{\text{meas}}\underline{\text{TAS}}_{\text{NED}}^{\text{no turb}} + \underline{\Delta} \tag{16}$$

$$\alpha = \arctan\left(\frac{w}{u}\right) \qquad \beta = \arcsin\left(\frac{v}{\text{TAS}}\right) \qquad M = \frac{\text{TAS}}{\sqrt{\gamma R T_s^{\text{forecast}}}} \tag{17}$$

$$\underline{w} = (\,\underline{w}_{a_{\text{NED}}} \quad w_{\delta_e} \quad w_{\delta_n} \quad w_{\Delta_u} \quad w_{\Delta_v} \quad w_{\Delta_w} \quad w_{\Delta_{v1}} \quad w_{\Delta_{w1}}\,)^T$$

and $\underline{v} = (\,\underline{v}_{V_{\text{NED}}} \quad \underline{v}_{ng_{\text{body}}}\,)^T$ are uncorrelated white Gaussian noises with zero mean and covariance functions $\underline{Q}(t_1, t_2) = \underline{Q}'\delta(t_1 - t_2)$ and $\underline{R}(t_1, t_2) = \underline{R}'\delta(t_1 - t_2)$, respectively. Furthermore, Δv_1 and Δw_1 are additional state variables because the Dryden turbulence is described by a second-order model concerning the v and w components [see Eq. (31)].

The inputs to the model come from real and virtual sensors:

$$\underline{u} = \underline{u}^{\text{meas}} = \begin{pmatrix} \text{Eul}^{\text{meas}} \\ \underline{W}_{\text{NE}}^{\text{forecast}} \\ p_s^{\text{forecast}} \\ T_s^{\text{forecast}} \\ \delta_{\text{elev}} \\ \delta_{\text{rud}} \\ g^{\text{WGS84}} \\ \underline{\omega}_{\text{body}}^{\text{meas}} \\ H^{\text{meas}} \end{pmatrix} \tag{18}$$

Note that in a first approximation the dynamic derivatives might be neglected: in this case, the angular-rate measurements are not required by the filter.

The measurement vector is composed of inertial quantities only:

$$\underline{z} = \underline{z}^{\text{meas}} = \begin{pmatrix} \underline{V}_{\text{NED}}^{\text{meas}} \\ \underline{ng}_{\text{body}}^{\text{meas}} \end{pmatrix} \tag{19}$$

Inertial velocity measurements can be obtained through an integration of the output of the accelerometers, $\underline{ng}_{\text{body}}$, for which the accuracy has been experimentally determined in our laboratories.

A. Extended Kalman Filter

The state equations of the Kalman filter [Eqs. (8) and (9)] are highly nonlinear, and therefore a local linear approximation along the trajectory becomes necessary to use the classical theory of a Kalman filter [19]. In particular, an extended Kalman filter (EKF) has been used. This kind of KF computes the linearized system starting from the state estimation and input vector at the previous step [20]. Note that the linear approximation will be quite accurate because it is updated with a computational frequency (100 Hz) much greater than the typical flight dynamics' frequency bandwidth. The only disadvantage of this approach is the necessity of performing an analytical linearization, because a numerical linearization would imply a computational effort unsuitable for a real-time application.

The state and measurement vector of a nonlinear discrete time system with additive noises ($\underline{w}_k$ and $\underline{v}_k$) can be expressed as

$$\begin{cases} \underline{x}_{k+1} = f(\underline{x}_k, \underline{u}_k) + \underline{w}_k \\ \underline{z}_k = h(\underline{x}_k, \underline{u}_k) + \underline{v}_k \end{cases} \tag{20}$$

The linearized equations of the preceding system, evaluated in the state estimation at the previous time step, are

$$\begin{cases} \bar{x}_{k+1} = f(\hat{x}_k, \underline{u}_k) \\ \bar{z}_k = h(\bar{x}_k, \underline{u}_k) \end{cases} \tag{21}$$

$$\begin{cases} \underline{x}_{k+1} \approx \bar{x}_{k+1} + \underline{A}(\underline{x}_k - \hat{x}_k) + \underline{w}_k \\ \underline{z}_k \approx \bar{z}_k + \underline{H}(\underline{x}_k - \bar{x}_k) + \underline{v}_k \end{cases} \tag{22}$$

where

$$\underline{A}_k = \frac{\partial f_i}{\partial x_j}(\hat{x}_k, \underline{u}_k)$$

is the Jacobian matrix of partial derivatives of f_i with respect to x_j,

$$\underline{H}_k = \frac{\partial h_i}{\partial x_j}(\bar{x}_k, \underline{u}_k)$$

is the Jacobian matrix of partial derivatives of h_i with respect to x_j, and $\underline{w}_k$ and $\underline{v}_k$ are uncorrelated white Gaussian noises with zero mean and diagonal covariance matrices $\underline{Q}_k$ and $\underline{R}_k$, respectively. The relationship between the covariance matrices $\underline{Q}_k$ and $\underline{R}_k$ and $\underline{Q}'$ and $\underline{R}'$ can be easily achieved by considering a sampling time T_c small enough, thus obtaining [20]

$$\underline{Q}_k \cong \underline{Q}' T_c \qquad \underline{R}_k \cong \underline{R}'/T_c \tag{23'}$$

B. Neural-Network-Based Aerodynamic Model

Analytical linearization of the system requires the knowledge of an analytical form of all the relationships that describe the system. Unfortunately, in our model, the aerodynamic coefficients are expressed in a tabular form as a function of several parameters. To overcome this limitation, an analytical relationship has been determined using an approach based on feedforward neural networks [21,22].

Let us consider the structure of each aerodynamic coefficient C_i^{ADB} in more detail:

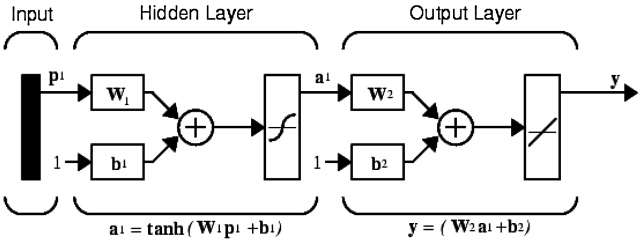

Fig. 4 Structure of the two-layer feedforward neural network.

$$C_i^{\text{ADB}}(M, Re, \alpha, \beta, \delta_{\text{elev}}^r, \delta_{\text{elev}}^l, \delta_{\text{rud}}, \underline{\omega}_{\text{body}}) = C_i^{\text{BL}} + \Delta C_i^{\beta} + \Delta C_i^{\delta_e} + \Delta C_i^{\delta_l} + \Delta C_i^{p} + \Delta C_i^{q} + \Delta C_i^{r} \tag{24}$$

Essentially, each C_i^{ADB} is a summation of a baseline term (BL) and other contributions due to the effect of other aerodynamic parameters. The term C_i^{BL} represents the baseline contribution to the global coefficient C_i^{ADB} at zero sideslip in a clean configuration (i.e., with no deflection of control surfaces and with no dynamic effects [23]). The term ΔC_i^j is the incremental coefficient due to a variation of the parameter j in a clean configuration and at zero sideslip (except, of course, when $j = \beta$). A detailed description of the database can be found in [23].

All of the terms C_i^{BL} and ΔC_i^j (hereinafter called c_i) are in the form of lookup tables as a function of the Mach number, Reynolds number, angle of attack (AOA), and other parameters [angle of sideslip (AOS), elevon deflections, or rudder deflections, according to the coefficient considered].

To derive an analytical characterization of each lookup table, training has been carried out on as many feedforward neural networks as the number of c_i. Each neural network had the same structure in terms of number of neurons, layers, and activation functions.

Figure 4 schematically shows the structure of each network. There are two layers: the hidden layer has 8 neurons and uses an hyperbolic tangent activation function, and the output layer uses a linear activation function. The number of input parameters $\underline{p}$ varies according to the c_i considered, as a consequence of the different functional dependencies of each term.

The training was carried out via a backpropagation technique using a comprehensive set of training pairs. Each pair consisted of a set of input/output values covering the entire set of lookup table breakpoints. Once trained (i.e., once the weights and the biases $\underline{W}_1$ are completely determined), the output of the network described in Fig. 4 can be easily computed analytically:

$$c_i = \underline{w}_{2i} \cdot \tanh(\underline{W}_{1i}\underline{p}_i + \underline{b}_{1i}) + b_{2i} \tag{25}$$

And it is equally easy to compute its derivative with respect to any of the state variables, upon which the parameters $\underline{p}$ are dependent. Of course, the terms c_i depend on the state variables through $\underline{p}$, and so

$$\frac{\partial c_i}{\partial \underline{x}} = \frac{\partial c_i}{\partial \underline{p}_i}\frac{\partial \underline{p}_i}{\partial \underline{x}} \tag{26}$$

Finally, the aerodynamic coefficients can be analytically written as

$$C_i^{\text{ADB}} = \sum c_i = \sum [\underline{w}_{2i} \cdot \tanh(\underline{W}_{1i}\underline{p}_i + \underline{b}_{1i}) + b_{2i}] \tag{27}$$

Consequently, their derivatives are

$$\frac{\partial C_i^{\text{ADB}}}{\partial \underline{x}} = \sum \frac{\partial c_i}{\partial \underline{x}} = \sum \left\{ \frac{\partial c_i}{\partial \underline{p}_i}\frac{\partial \underline{p}_i}{\partial \underline{x}} \right\} = \sum \left\{ \frac{\partial}{\partial \underline{p}_j}[\underline{w}_{2i} \cdot \tanh(\underline{W}_{1i}\underline{p}_i + \underline{b}_{1i}) + b_{2i}]\frac{\partial \underline{p}_i}{\partial \underline{x}} \right\} \tag{28}$$

It was verified that the approximation error introduced by the neural network on the aerodynamic coefficients is on the order of 2–3%, which is an acceptable degree of accuracy as far as the objectives

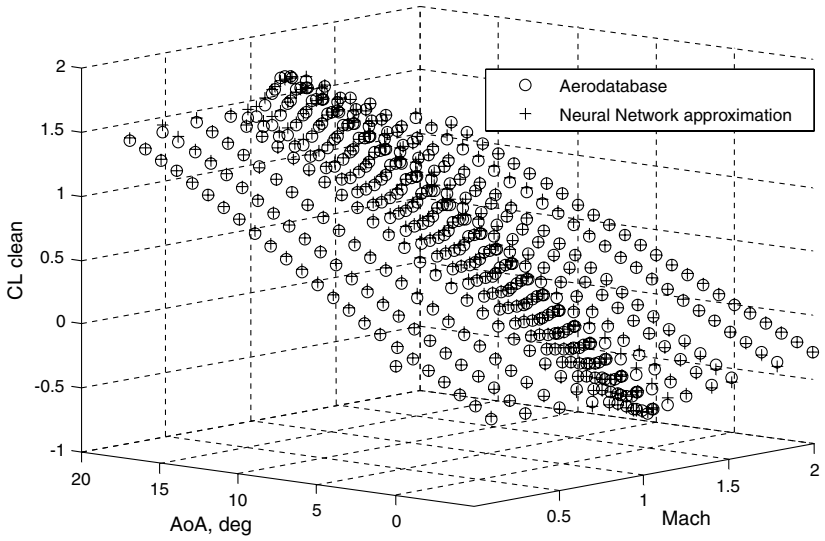

Fig. 5 An example of the approximation of an ADB aerodynamic coefficient using neural network approach.

of this work are concerned. Figure 5 reports an example of the approximation of an ADB aerodynamic coefficient using the neural network approach.

C. Process Noise Characterization

As previously said, the dynamic state Eq. (8) takes into account unmodeled dynamics and parameter uncertainties through the random vector $\underline{w}(t)$, and the measurement Eq. (9) takes into account the measurement errors through the random vector $\underline{v}(t)$.

Concerning the tuning of the elements of covariance matrix $\underline{Q}'$ corresponding to $\underline{w}_{a_{\text{NED}}}$ (that is, $\sigma^2_{w_{a_{\text{NED}}}}$), a Monte Carlo analysis [24] (with reference to the DTFT mission of interest) has been performed considering all the sources of uncertainties (i.e., ADB uncertainties; neural network ADB approximation; WGS84 gravity-acceleration error model; and measurement errors on angular rates, Euler angles, and control surfaces deflections).

The elements of $\underline{Q}'$ related to the Gauss–Markov wind forecast error models $\sigma^2_{w_{\delta e}}$ and $\sigma^2_{w_{\delta n}}$ are computed, recalling that these errors are obtained by passing white noise w_{δ_e} and w_{δ_n} with variances $\sigma_1^2 = \sigma^2_{\delta_e}(2/\tau_{\delta_e})$ and $\sigma_2^2 = \sigma^2_{\delta_n}(2/\tau_{\delta_n})$ through the filters $H_{\delta_e}(j\omega)$ and $H_{\delta_n}(j\omega)$ [see Eqs. (3)] having the following equations:

$$\frac{d\delta_e}{dt} = -\frac{\delta_e}{\tau_{\delta_e}} + w_{\delta_e} \qquad \frac{d\delta_n}{dt} = -\frac{\delta_n}{\tau_{\delta_e}} + w_{\delta_n} \tag{29}$$

which have the same form of Eq. (8), then we can simply put $\sigma^2_{w_{\delta e}} = \sigma^2_{\delta_e}(2/\tau_{\delta_e})$ and $\sigma^2_{w_{\delta n}} = \sigma^2_{\delta_n}(2/\tau_{\delta_n})$ [see Eq. (3)].

The elements of $\underline{Q}'$ related to the turbulence model are computed, recalling that these errors are obtained by passing a generic white noise n with variances $\sigma_n^2 = \bar{\sigma}^2(2\tau_\Delta/\pi)$, through the filters $H_{\Delta u}(\omega)$, $H_{\Delta v}(\omega)$, and $H_{\Delta w}(\omega)$, respectively [see Eq. (7)]. $H_{\Delta u}(\omega)$ has the state-space equation

$$\frac{d\Delta u}{dt} = -\frac{\Delta u}{\tau_\Delta} + \frac{n}{\tau_\Delta} \tag{30}$$

and $H_{\Delta v}(\omega)$ and $H_{\Delta w}(\omega)$ have the following second-order equations:

$$\frac{d\Delta v_1}{dt} = -\frac{\Delta v_1}{\tau_\Delta} + \frac{n}{\tau_\Delta}$$

$$\frac{d\Delta v}{dt} = -\frac{\Delta v}{\tau_\Delta} + \left(\frac{1-\sqrt{3}}{\tau_\Delta}\right)\Delta v_1 + \sqrt{3}\frac{n}{\tau_\Delta}$$

$$\frac{d\Delta w_1}{dt} = -\frac{\Delta w_1}{\tau_\Delta} + \frac{n}{\tau_\Delta}$$

$$\frac{d\Delta w}{dt} = -\frac{\Delta w}{\tau_\Delta} + \left(\frac{1-\sqrt{3}}{\tau_\Delta}\right)\Delta w_1 + \sqrt{3}\frac{n}{\tau_\Delta} \tag{31}$$

which have the same form of Eq. (8), provided that

$$w_{\Delta u} = \frac{n}{\tau_\Delta} \quad w_{\Delta v} = \frac{\sqrt{3}n}{\tau_\Delta} \quad w_{\Delta w} = \frac{\sqrt{3}n}{\tau_\Delta} \quad w_{\Delta v_1} = \frac{n}{\tau_\Delta}$$

$$w_{\Delta w_1} = \frac{n}{\tau_\Delta}$$

Therefore, combining Eqs. (8), (30), and (31), the following noise variances are obtained:

$$w_{\Delta u} = \frac{n}{\tau_\Delta} \Rightarrow \sigma^2_{w_{\Delta u}} = \frac{2\bar{\sigma}^2}{\pi}\frac{1}{\tau_\Delta} \qquad w_{\Delta v} = \frac{\sqrt{3}n}{\tau_\Delta} \Rightarrow \sigma^2_{w_{\Delta v}} = 3\frac{\bar{\sigma}^2}{\pi}\frac{1}{\tau_\Delta}$$

$$w_{\Delta w} = \frac{\sqrt{3}n}{\tau_\Delta} \Rightarrow \sigma^2_{w_{\Delta w}} = 3\frac{\bar{\sigma}^2}{\pi}\frac{1}{\tau_\Delta} \qquad w_{\Delta v_1} = \frac{n}{\tau_\Delta} \Rightarrow \sigma^2_{w_{\Delta v1}} = \frac{\bar{\sigma}^2}{\pi}\frac{1}{\tau_\Delta}$$

$$w_{\Delta w_1} = \frac{n}{\tau_\Delta} \Rightarrow \sigma^2_{w_{\Delta w1}} = \frac{\bar{\sigma}^2}{\pi}\frac{1}{\tau_\Delta} \tag{32}$$

Finally, the covariance matrix $\underline{R}'$ is defined by the accelerometers' accuracy (experimentally determined) and the related velocities' accuracy.

V. Results

Some relevant results of this work are reported in this section and are referred to as the DTFT missions [12]. In particular, a verification of the VAD algorithm was carried out using the flight data of the DTFT1 mission.

The VAD algorithms provide the complete set of air data, including angles of attack and sideslip and Mach number [see Eq. (17)], together with other quantities (air temperature, static and total air pressure, barometric altitude, etc.). In this section, only the flow angles and the Mach number will be reported, because these quantities are strictly related to the TAS vector for which the estimation is the main objective of the VAD sensor fusion.

During the DTFT1 mission, these measured air data were provided by two wind vanes and static and total pressure probes. The declared static accuracies for these three basic measurements are reported in Table 1. Therefore, it can be assumed that the *true* air data are contained within these uncertainties bounds.

The basic inertial sensor unit for the DTFT missions is composed by microelectromechanical system accelerometers (bias ≈ 0.015 m/s^2) and by fiber optical gyros (bias ≈ 3 deg/h). The accelerometers are used to compute inertial velocity using Euler-angle information provided by the AHRS module. Note that the velocity drift is not of concern because of the short time ranges of the DTFT missions; therefore, no additional measurement (i.e., Global Positioning System) is required.

Table 1 Declared static accuracies for the measured air data

Measured air data	Maximum error	Additional notes
AOA	0.5 deg	In addition, there is an additive positioning error, evaluated by means of CFD analysis.
AOS	0.5 deg	N/A
M	0.01	The sensor is declared calibrated only for $0.2 < M < 0.9$; in particular, no specific calibration was carried out in the transonic region.

The results here reported are related to the DTFT flight envelopes; thus, the analysis carried out is limited to the transonic region. Further studies are required to also numerically validate the VAD approach in the supersonic and hypersonic regions.

In the following, the results of the VAD sensor fusion will be shown, also putting in evidence that the application of the EKF (advanced VAD) improves the accuracy of the computation of the air data with respect to a simple algebraic composition of inertial measurements and weather forecast data (basic VAD) (see Sec. II).

In the DTFT1 mission, the FTB1 vehicle was dropped (with nose down) from an altitude of about 20 km and performed a controlled flight with a constant angle of attack to reach a Mach value of 1.05 before slowing down. Figure 6 shows the virtual angle of attack computed using the −18 h forecast meteorological information (without EKF) with respect to the measured AOA, affected by the white noise measurement specified in Table 1. Note that the −18 h forecast represents the most reliable meteorological information available for the DTFT1 mission. In fact, even if during the flight campaign some soundings were carried out at the site of launch, the last sounding available was carried out about 6 h before the launch. However, it was shown in [15] that these soundings are less reliable at predicting the wind behavior than the wind forecast data relative to 18 h before the launch. This is why the −18 h wind forecast data have been used to construct the wind model used by the VAD system.

Figure 6 also reports the inertial estimation of the AOA: that is, the estimation of the angle of attack made using inertial measurements only. The figure shows that the basic VAD estimation is much more accurate than the inertial estimation, especially when inertial and wind velocities are comparable. However, there are still significant estimation errors, mainly due to unmodeled prediction errors and to unsteady local phenomena. This limitation can also be overcome using the measured load factors and appropriate mathematical models for the wind prediction error, turbulence, and vehicle aerodynamics.

During the initial seconds of flight (0–15 s) the true air speed is relatively low; as a consequence, because the wind vanes are a very low damped mechanical system, the measured flow angles exhibit large oscillations. Conversely, the virtual data cannot be affected by this problem, as shown in Fig. 7.

As it can be seen in Fig. 8, after 20 s from the drop, the virtual sideslip angle becomes significantly different from the vane measurement principally as a consequence of a low-frequency wind forecast error, which is not taken into account. This effect is more evident on the sideslip angle rather than on the AOA, because AOS values are closer to zero.

Figure 9 shows other relevant advantages of the VAD approach. In the transonic regime, it is usually necessary to carry out an experimental calibration of the air data to take into account compressibility effects. In the case of the DTFT1 mission, no specific calibration was carried out (see Table 1), leading to a measured Mach number less reliable than the virtual one. Moreover, as can be seen, the virtual Mach is not influenced by lower saturations affecting the pressure transducers or other sensors.

Now let us consider the VAD with the EKF sensor fusion approach: the introduction of the wind forecast error model and of the turbulence model significantly improves the air data estimation that now also includes the effects of the high-frequency wind phenomena (see Figs. 10 and 11).

In Fig. 10, the estimated AOA is reported. It can be seen that the estimation is very close to the vane measurement. The main reason for this good result is that the relationship between the measured load factors, and the air data has been explicitly taken into account through the aerodynamic model [Eq. (14)].

In the transonic region ($t \approx 32$ s), the angle of attack evidences a rapid pitch-down phenomenon. In such a case, static accuracies reported in Table 1 are not properly applicable. As a consequence, no specific consideration can be made about the performance of the VAD in this particular flight phase.

The estimated AOS (Fig. 11) is generally within the measurement uncertainty bounds in the whole time span in which it is reasonable to consider the vane measurements as valid (i.e., after 15 s from the drop). Around 26 s, the estimated AOS is slightly out of the vane measurement bounds. However, this behavior is in agreement with the measurement of the lateral load factor (see Fig. 12).

In Fig. 13, the estimated Mach number is reported: note that it is quite similar to that obtained using the basic VAD approach (see Fig. 9). In fact, the Mach number is less sensitive to wind and turbulence disturbances than the flow angles, because it only depends

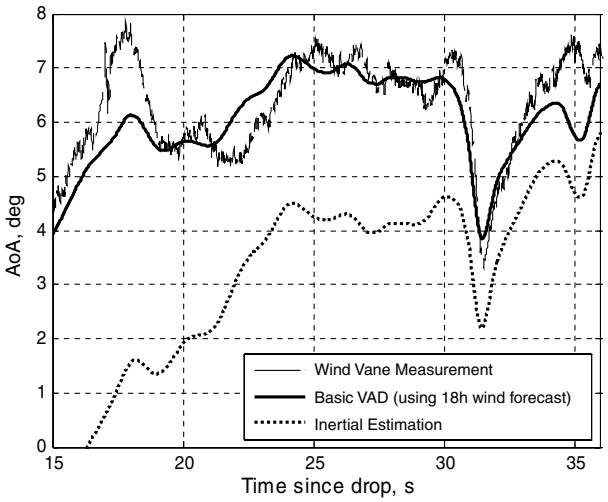

Fig. 6 Comparison of the virtual AOA computed without EKF (basic VAD) using the 18 h wind forecast data with the actual vane measurement and the inertial estimation.

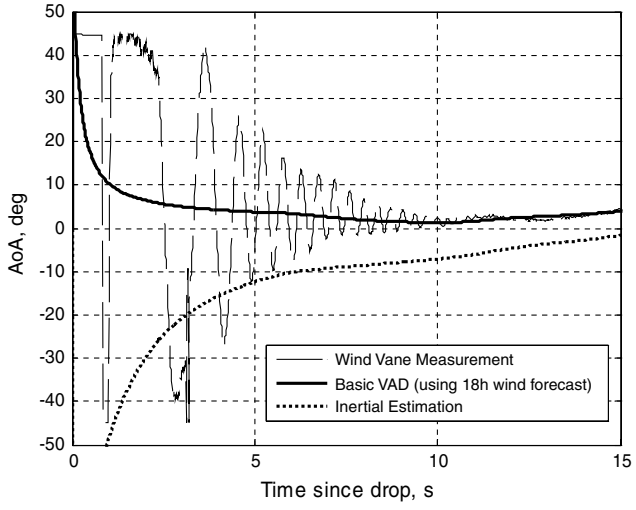

Fig. 7 Undamped behavior of wind vane measurement.

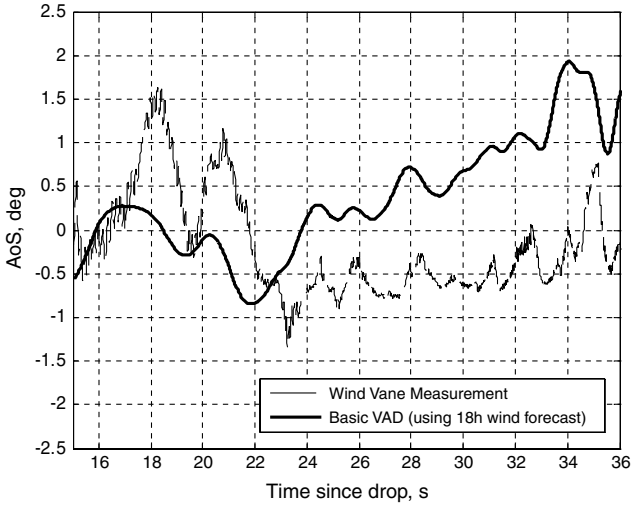

Fig. 8 Comparison of the virtual AOS computed without EKF (basic VAD) using the 18 h wind forecast data with the actual vane measurement.

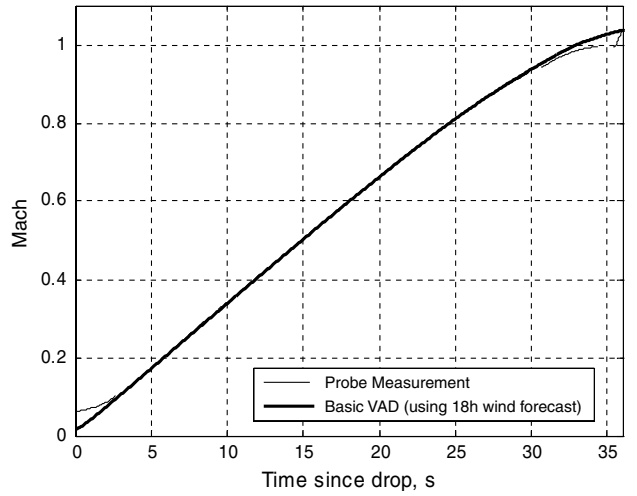

Fig. 9 Comparison of the virtual Mach computed without EKF (basic VAD) using the 18 h wind forecast data with the actual probe measurement.

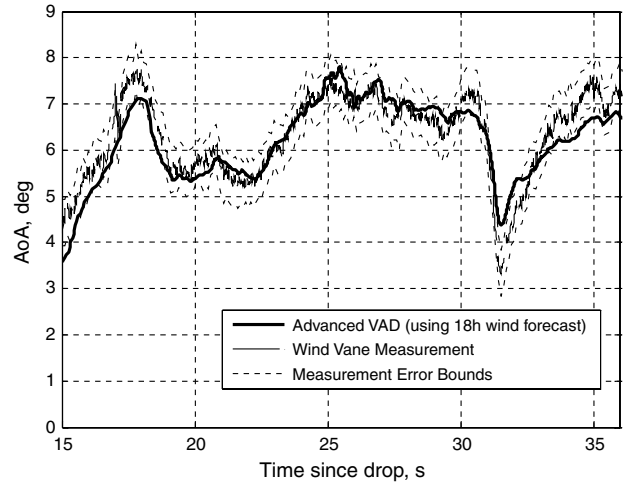

Fig. 10 Comparison of the virtual AOA computed with the EKF (advanced VAD) using the 18 h wind forecast data with the actual vane measurement together with the declared uncertainty bounds.

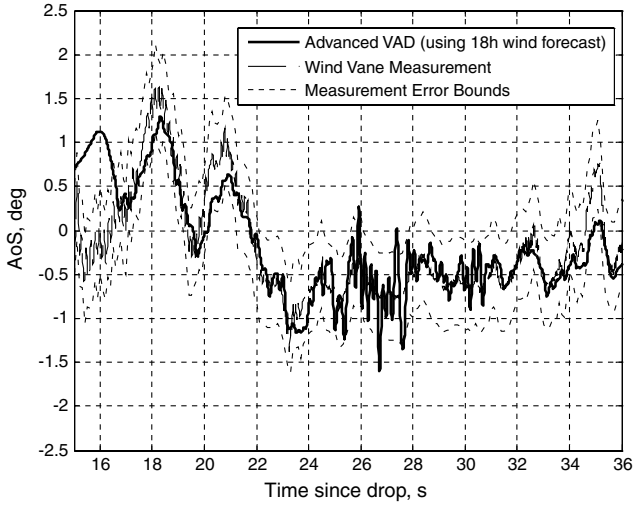

Fig. 11 Comparison of the virtual AOS computed with the EKF (advanced VAD) using the 18 h wind forecast data with the actual vane measurement together with the declared uncertainty bounds.

on the module of the true-air-speed vector, whereas the flow angles depend on the body components of the TAS.

In the transonic region (i.e., after 30 s from the drop), the ADB uncertainties increase noticeably and the VAD are estimated, improving the relative trust to inertial measurements with respect to the mathematical models. In any case, no reliable data accuracies are available for the air data measurements in this regime.

Note that all the reported results are obtained using the −18 h weather forecast data and the related Gauss–Markov model of the ECMWF wind prediction error. If this meteorological information is

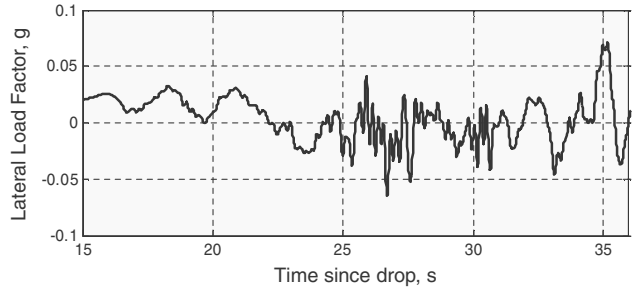

Fig. 12 Lateral load factor measurement.

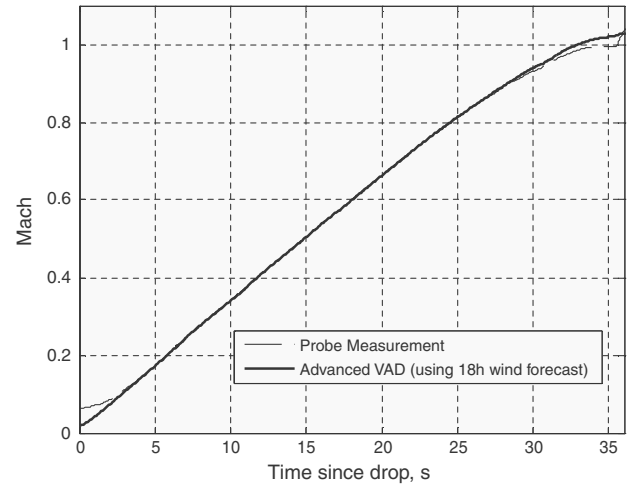

Fig. 13 Comparison of the virtual Mach computed with the EKF (advanced VAD) using the 18 h wind forecast data with the actual probe measurement.

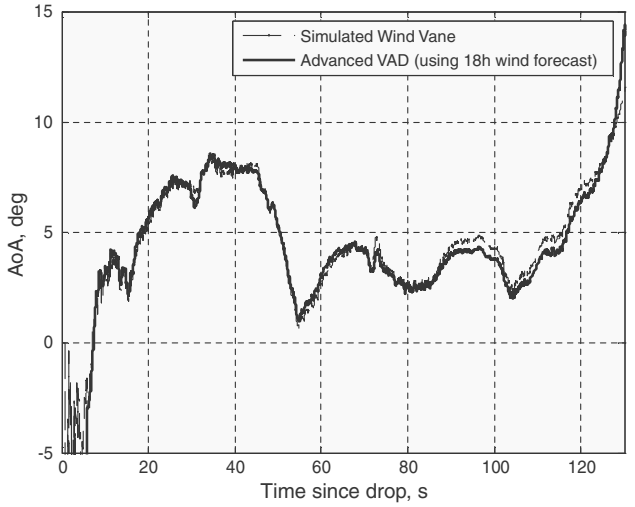

Fig. 14 Comparison of the virtual AOA computed with the EKF (advanced VAD) using the 18 h wind forecast data with the simulated vane measurement for the DTFT2 mission.

not available, a less recent forecast may be used in combination with a different error model that accounts for the lower reliability of the forecast. In any case, the unsteady phenomena will always be well taken into account by the Dryden turbulence model (as explained in Sec. III).

The DTFT2 mission, currently scheduled for the end of 2009, aims at extending and improving the investigation of the transonic regime of flight, from both the aerostructural and the stability and control points of view. The DTFT2 mission objective is to perform a controlled acceleration phase (after the vehicle drop at 24 km of altitude) with a constant angle of attack followed by an angle-of-attack sweep maneuver at constant Mach number in the transonic flight regime before slowing down the vehicle to the minimum attainable Mach value (necessary condition for the safe opening of the recovery parachute).

For the results concerning this mission, measurements are obtained through a simulation environment that uses the ADB identified during the DTFT1 postflight analysis [25], reference wind profiles, and gust and turbulence simulation models. For simplicity, only the results related to the advanced VAD are presented, because this algorithm will be implemented in the upcoming DTFT2 mission.

The results shown in Figs. 14–16 essentially demonstrate that the EKF process noise characterization performed for the DTFT2 mission (related to a significantly different flight trajectory) still gives satisfactory results.

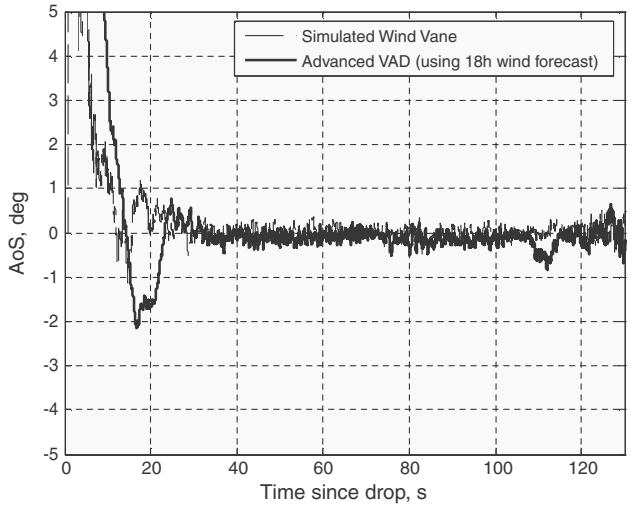

Fig. 15 Comparison of the virtual AOS computed with the EKF (advanced VAD) using the 18 h wind forecast data with the simulated vane measurement for the DTFT2 mission.

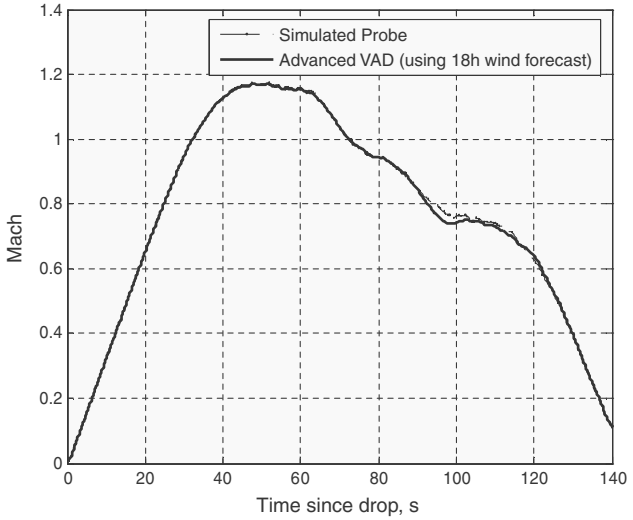

Fig. 16 Comparison of the virtual Mach computed with the EKF (advanced VAD) using the 18 h wind forecast data with the simulated probe measurement for the DTFT2 mission.

VI. Future Enhancements

The results of the virtual air data approach presented in Sec. V appear to be promising and encouraging for flight applications. Of course, further improvements on its architecture will be considered as a part of future work. Current work is focusing on the implementation of the VAD for in-flight use as the main air data sensor system for guidance and control feedback during the DTFT2 mission. In any case, the VAD architecture appears to be suitable as an effective backup system for real ADS. In this case, the VAD sensor fusion algorithm could be made more reliable and accurate through in-flight and online training of the neural network that approximates the aerodatabase (the training should be carried out, of course, before the ADS failure). This online training procedure would therefore provide a more accurate aerodatabase for the computation of the VAD when needed.

Finally, the authors believe that the VAD approach could eventually allow full replacement of current air data systems, provided that further studies demonstrate sufficient reliability of the algorithm and of the weather forecast data in typical reentry flight regimes. In addition, future USV missions will assess the effectiveness of the VAD in supersonic and hypersonic flight envelopes.

VII. Conclusions

An innovative air data system architecture has been developed based on the concept of virtual air data. This novel approach combines weather forecast data with inertial measurements and does not require any air data sensor. In fact, the true-air-speed components are estimated through an extended Kalman filter, which also requires a turbulence model and an ADB model. As a matter of fact, the results presented in this work appear to be highly satisfactory and promising. Indeed, this approach may effectively work as a backup solution for conventional air data systems when an ADS failure occurs. In addition, the VAD architecture appears to be a viable solution to overcome the common limitations of the conventional air data systems, eventually replacing real air data sensors when the feasibility and reliability of the presented approach will be fully demonstrated.

The effectiveness of the proposed architecture has been demonstrated, comparing the air data estimation with the flight data of CIRA's DTFT1 mission. The algorithm was also validated in a specific simulation environment for the DTFT2 mission and will be used onboard as the main DTFT2 air data sensor system for GN&C purposes.

References

[1] Kayton, M., and Fried, W. R., *Avionics Navigation Systems*, Wiley, New York, 1997.

[2] Pruett, C. D., Wolf, H., Heck, M. L., and Siemers, P. M., III, "Innovative Air Data System for the Space Shuttle Orbiter," *Journal of Spacecraft and Rockets*, Vol. 20, No. 1, 1983, pp. 61–69. doi:10.2514/3.28357

[3] Cary, J. P., and Keener, E. R., "Flight Evaluation of the X-15 Ball-Nose Flow-Direction Sensor as an Air-Data System," NASA TN D-2923, 1965.

[4] Wolowicz, C. H., and Gossett, T. D., "Operational and Performance Characteristics of the X-15 Spherical, Hypersonic Flow-Direction Sensor," NASA TN D-3070, 1965.

[5] Ellsworth, J. C., and Whitmore, S. A., "Simulation of a Flush Air-Data System for Transatmospheric Vehicles," *Journal of Spacecraft and Rockets*, Vol. 45, No. 4, 2008, pp. 716–732. doi:10.2514/1.33541

[6] Moes, T. R., and Whitmore, S. A., "A Preliminary Look at Techniques Used to Obtain Air Data from Flight at High Angles of Attack," NASA TM-101729, 1990.

[7] Whitmore, S. A., Cobleigh, B. R., and Haering, E. A., "Design and Calibration of the X-33 Flush Air Data Sensing (FADS) System," NASA Dryden Flight Research Center, TM-1998-206540, Edwards, AFB, CA, 1998.

[8] Cobleigh, B. R., Whitmore, S. A., Haering, E. A., Borrer, J., and Roback, V. E., "Flush Air Data Sensisng (FADS) System Calibration Procedures and Results for Blunt Forebodies," NASA TP 1999-209012.

[9] Davis, M. C., Pahle, J. W., White, J. T., Marshall, L. A., Mashburn, M. J., and Franks, R., "Development of a Flush Air Data Sensing System on a Sharp-Nosed Vehicle for Flight at Mach 3 to 8," NASA TM-209017, 2000.

[10] Bogue, R. K., and Jentink, H. W., "Optical Air Flow Measurement in Flight," NASA TP-2004-210735, 2004.

[11] Jentink, H. W., and Bogue, R. K., "Optical Air Flow Measurements for Flight Tests and Flight Testing Optical Flow Meters," National Aerospace Lab., TP-2005-256, Amsterdam, 2005.

[12] Russo, G., Carmicino, C., de Matteis, P., Marini, M., Rufolo, G., Di Palma, L., Belardo, M., Corraro, F., and Verde, L., "Unmanned Space Vehicle Program: DTFT in Flight Experiments," *18th ESA Symposium on European Rocket Programmes and Related Research, ESA Communication Production Office*, European Space Research and Technology Centre, Noordwijk, The Netherlands, Nov. 2007, pp. 89–96.

[13] Russo, G., and de Matteis, P. P., "PRORA-USV: Two Flight Mission Exploring Transonic Conditions", 15th AIAA International Space Planes and Hypersonic Systems and Technologies Conference, Dayton, OH, AIAA Paper 2008-2660, 2008.

[14] Palumbo, R., Russo, M., Filippone, E., and Corraro, F., "ACHAB: Analysis Code for High-Altitude Balloons," AIAA Atmospheric Flight Mechanics Conference and Exhibit, AIAA Paper 2007-6642, Hilton Head, SC, 2007.

[15] Morani, G., Palumbo, R., Cuciniello, G., Corraro, F., and Russo, M., "Method for Prediction and Optimization of a Stratospheric Balloon Ascent Trajectory," *Journal of Spacecraft and Rockets*, Vol. 46, No. 1, 2009, pp. 126–133. doi:10.2514/1.39469

[16] Merhav, S., *Aerospace Sensor Systems and Applications*, Springer–Verlag, New York, 1996.

[17] Singer, R. A., "Estimating Optimal Tracking Filter Performance for Manned Maneuvering Targets," *IEEE Transactions on Aerospace and Electronic Systems*, Vol. 6, No. 4, 1970, pp. 473–483. doi:10.1109/TAES.1970.310128

[18] "Flying Qualities of Piloted Airplanes," MIL-F-8785C, U.S. Navy, U.S. Dept. of Defense, Nov. 1980.

[19] Kalman, R. E., "A New Approach to Linear Filtering and Prediction Problems," *Transactions of the ASME, Series D: Journal of Basic Engineering*, Vol. 82, Mar. 1960, pp. 35–45; available online at http://www.cs.unc.edu/~welch/kalman/media/pdf/Kalman1960.pdf.

[20] Gelb, A., *Applied Optimal Estimation*, M.I.T. Press, Cambridge, MA, 1989.

[21] Cruciani, I., De Divitiis, N., De Matteis, G., and Filippone, E., "Autonomous Guidance for a Sub-Orbital Re-Entry Vehicle," 54th International Astronautical Congress, Paper IAC-03-A.7.06, Bremen, Germany, 2003.

[22] McMillen, R. L., Steck, J. E., and Rokhsaz, K., "Application of an Artificial Neural Network as a Flight Test Data Estimator," *Journal of Aircraft*, Vol. 32, No. 5, 1995, pp. 1088–1094. doi:10.2514/3.46840

[23] Rufolo, G. C., Roncioni, P., Marini, M., and Votta, R., "Experimental and Numerical Aerodynamic Data Integration and Aerodatabase Development for the PRORA-USV-FTB_1 Reusable Vehicle," 14th AIAA/AHI International Space Planes and Hypersonic System and Technology Conference, Canberra, Australia, AIAA Paper 2006-8031, 2006.

[24] Corraro, F., Filippone, E., Russo, M., and Morani, G., "A Monte Carlo Based Analysis for USV FTB_1 DTFT Mission Validation," 14th AIAA/AHI International Space Planes and Hypersonic System and Technology Conference, Canberra, Australia, AIAA Paper 2006-8015, 2006.

[25] Vitale, A., Cuciniello, G., Nebula, F., Russo, M., and Corraro, F., "Post Flight Data Analysis of guidance, navigation, and control Experiment for DTFT1 Mission," *2nd International ARA Days: "10 years After ARD"*, Paper AA-3-2008-58, Bordeaux, France, 2008.

J. Martin
Associate Editor